Tailoring magnetic energies to form dipole skyrmions and skyrmion lattices

S. A. Montoya,[1,2] S. Couture,[1,2] J. J. Chess,[3] J. C. T. Lee,[3,4] N. Kent,[5] D. Henze,[5] S. K. Sinha,[6] M.-Y. Im,[4,7] S. D. Kevan,[3,4] P. Fischer,[4,5] B. J. McMorran,[3] V. Lomakin,[1,2] S. Roy,[4] and E. E. Fullerton[1,2,*]

[1]*Center for Memory and Recording Research, University of California–San Diego, La Jolla, California 92093, USA*
[2]*Department of Electrical and Computer Engineering, University of California–San Diego, La Jolla, California 92093, USA*
[3]*Department of Physics, University of Oregon, Eugene, Oregon 97401, USA*
[4]*Center for X-ray Optics, Lawrence Berkeley National Laboratory, Berkeley, California 94720, USA*
[5]*Physics Department, University of California, Santa Cruz, California 94056, USA*
[6]*Department of Physics, University of California–San Diego, La Jolla, California 92093, USA*
[7]*Department of Emerging Materials Science, Daegu Gyeongbuk Institute of Science and Technology, Daegu, Korea*

(Received 12 August 2016; revised manuscript received 28 October 2016; published 13 January 2017)

The interesting physics and potential memory technologies resulting from topologically protected spin textures such as skyrmions have prompted efforts to discover new material systems that can host these kinds of magnetic structures. Here, we use the highly tunable magnetic properties of amorphous Fe/Gd multilayer films to explore the magnetic properties that lead to dipole-stabilized skyrmions and skyrmion lattices that form from the competition of dipolar field and exchange energy. Using both real space imaging and reciprocal space scattering techniques, we determined the range of material properties and magnetic fields where skyrmions form. Micromagnetic modeling closely matches our observation of small skyrmion features (∼50 to 70 nm) and suggests that these classes of skyrmions have a rich domain structure that is Bloch-like in the center of the film and more Néel-like towards each surface. Our results provide a pathway to engineer the formation and controllability of dipole skyrmion phases in a thin film geometry at different temperatures and magnetic fields.

DOI: 10.1103/PhysRevB.95.024415

I. INTRODUCTION

Skyrmions are topologically nontrivial cylindrical-like magnetic domains that exhibit novel physics and potential applications to nonvolatile memory [1–6]. Today, these textures exist in an array of materials from bulk magnets [7–10] to thin films [11–19], and they have been shown to be stable under several physical mechanisms [19–23]. The most heavily studied mechanism to stabilize skyrmions is the Dzyaloshinskii-Moriya interaction (DMI), arising in noncentrosymmetric magnetic materials or thin films with an asymmetric heavy metal interface [7–14]. However, topologically similar spin structures can be stabilized by the competition of long-range dipolar energy in a thin film geometry and domain wall energy [16–19], a mechanism by which magnetic stripes and bubbles form [24–40]. Commonly, a chiral magnetic bubble is termed a dipole-stabilized skyrmion because of the resemblance to a Bloch-type DM interaction skyrmion [2,17–19]. Given that these chiral bubbles form under the application of a perpendicular magnetic field, they are said to be extrinsically stable [5]. Both of these classes of topologically protected magnetic features are interesting, and there are numerous examples of materials showing them; however, there is a limited understanding of the basic magnetic energetics required to favor their formation. These chiral bubbles or dipole-stabilized skyrmions present a test-bed for exploring how the balance among ferromagnetic exchange, anisotropy, and dipolar energy results in cylindrical-like domains that are topologically nontrivial.

In this work, we explore the formation of dipole-stabilized skyrmions and skyrmion lattices in amorphous Fe/Gd multilayers, with the focus on developing predictive properties that can result in the stabilization of chiral textures. Through thickness, alloy composition, and temperature-dependent studies of various Fe/Gd films, we find we can control the skyrmion lattice, in temperature and applied magnetic fields, by tuning the material properties of the multilayer structure. This tunability allows us to investigate the skyrmion sensitivity to material properties to manifest ordered and disordered skyrmions. By comparing experimental findings with micromagnetic modeling, we show the skyrmion-lattice phase appears for a parameter space with a combination of relatively low perpendicular magnetic anisotropy (PMA) ($\sim 2-4 \times 10^5$ ergs/cm^3), low magnetic moment ($\sim 350-500$ emu/cm^3), low exchange interaction ($\sim 5 \times 10^{-7}$ ergs/cm), and thick films (>40 nm). Our results provide a guideline for the magnetic properties required to stabilize these spin textures in thin film ferromagnets and ferrimagnets.

The Fe/Gd films we studied consist of multilayer deposited structures of Fe and Gd thin films (each layer <0.4 nm), which are antiferromagnetically coupled, forming a ferrimagnet. By appropriately choosing the thickness of the layers and the deposition conditions, the films develop PMA [39–40]. In general, favorable conditions for the observation of perpendicular magnetic domains requires the uniaxial anisotropy K_U be greater than the shape anisotropy $K_D = 2\pi M_S^2$, where the ratio of these parameters is defined as a material's Q factor [25]. For our films, the Q ratios are less than 1, but by increasing the number of bilayer repetitions (i.e., the total film thickness) a transition from in-plane magnetization to the formation of perpendicular magnetic domains can be achieved [41–45]. We will first show Lorentz transmission electron microscopy (TEM), resonant soft x-ray scattering (SXS), and full-field transmission x-ray microscopy to confirm the presence of skyrmions and skyrmion lattices in our films and determine

*Corresponding author: efullerton@ucsd.edu

the sensitivity of the skyrmion formation to the temperature, applied magnetic field range, and film thickness. We will then quantify the materials parameters of our films and compare the experimental results to micromagnetic simulations.

II. METHODS

The Fe/Gd specimens were sputter deposited at room temperature in an ultrahigh vacuum (UHV) environment under a 3 mTorr argon environment. To grow the film structures, we alternatively deposited Fe and Gd layers of a specific thickness and continued the process until the desired number of layers was achieved. Films had a seed/capping layer of 5 nm Ta to protect the films from corrosion. Samples were deposited on a range of different substrates for magnetic and imaging characterization, including 50 nm and 200 nm SiN membranes and Si substrate with a native oxide layer.

The field and temperature dependence of the magnetic domain morphology was imaged using a variety of techniques, which include: (i) Lorentz TEM using an FEI Titan in Lorentz mode equipped with an image aberration corrector, (ii) SXS at the Gd M_5 (1198 eV) absorption edge and Fe L_3 (708 eV) absorption edge at Beamline 12.0.2 Advanced Light Source, Lawrence Berkeley National Laboratory, and (iii) full-field transmission x-ray microscopy along the Fe L_3 (708 eV) absorption edge performed at Beamline 6.1.2 Advanced Light Source, Lawrence Berkeley National Laboratory.

Magnetic hysteresis measurements were characterized using a Quantum Design PPMS cryostat with vibrating sample magnetometer and a magneto-optical Kerr effect magnetometer. The ferromagnetic resonance measurements were performed using a custom probe that affixes a coplanar waveguide at one end and can be inserted into a Quantum Design Physical Property Measurement System (PPMS) for temperature and direct current (dc) magnetic field H_{dc} probing. The radio frequency (RF) field h_{RF} lies in the plane to the magnetic film specimen, and H_{dc} is transverse to the coplanar waveguide. The ferromagnetic resonance is extracted from the reflection coefficients of scattering parameters using an Agilent PVNA E8363B in field-swept mode.

III. RESULTS

A. Skyrmion lattice formation at room temperature

Figure 1 shows the field dependence of the magnetic domain morphology of a [Fe (0.34 nm)/Gd (0.4 nm)] × 80 multilayer (total thickness 53.6 nm; see Supplemental Material, Section C [46]) imaged by means of a Lorentz TEM at room temperature. The underfocused images were obtained as a magnetic field perpendicular to the sample was swept from zero towards magnetic saturation. Each field image was from the same region of the sample, but not the same specific area of the sample, as the image position shifted with applied magnetic field. At zero field, the film exhibited stripe domains that have a periodicity of ∼124 nm [Fig. 1(a)] and random in-plane order. The images reveal the in-plane magnetization orientation averaged over the thickness of the magnetic domains through variations of darkness/brightness intensity, and domain walls are evidenced by strong and sharp dark/bright contrast changes. Analysis of over/underfocused

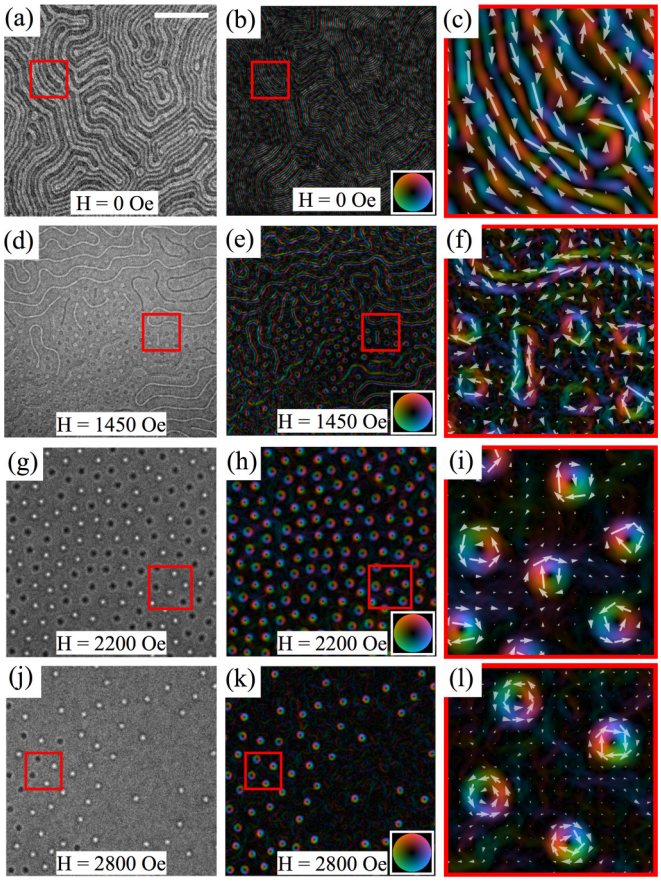

FIG. 1. Real space imaging of the field-dependent magnetic domain morphology of [Fe (0.34 nm)/Gd (0.4 nm)] × 80. Underfocused Lorentz TEM images (first column) measured at room temperature and their corresponding magnetic induction color maps (second column) are detailed. The images are captured as a perpendicular magnetic field is applied from zero field to magnetic saturation. Four different magnetic states are observed as the field is swept, including: disordered stripe domains (a, b), stripe-to-skyrmion transition (d, e), skyrmion lattice (g, h), and disordered skyrmions (j, k). Enclosed regions in the first two columns are enlarged to detail the in-plane magnetic domain configuration using both color and vector magnetic induction maps in the third column (c, f, i, l). The scale bar in (a) corresponds to 1 μm.

Lorentz TEM images using the transport-of-intensity equation [47,48] allows us to determine the projected in-plane magnetic induction, shown as a color map in Fig. 1(b). Here, the color indicates the direction of the magnetic induction with respect to the color-wheel insert; in a similar fashion, the color intensity details the magnitude of the magnetic induction. The images show that the stripe domains are separated by Bloch walls [Fig. 1(b)], where the in-plane moment of the walls is parallel to the stripes. This arrangement is more clearly observable in the enlarged image [Fig. 1(c)] detailing the enclosed region of Figs. 1(a) and 1(b), where both the color and vector maps detail the direction of the Bloch wall. Since the films are relatively thick, and no DMI is anticipated, a Bloch-like domain structure is expected. As will be discussed below, there are likely closure domains (e.g., Néel caps) at the top and bottom of the films [49]. Evidence of closure domains will not be visible in these

images, since the orientations of these domains at the top and bottom of the films are opposite in direction and will average to zero in Lorentz TEM images.

As a magnetic field is applied, perpendicular to the film [Figs. 1(d) and 1(e)], the stripes with magnetization parallel to the field grow at the expense of domains opposite to the field. We observe that the stripe domains for which the magnetization is opposite to the field begin to collapse into cylindrical domains [Figs. 1(d) and 1(e)]. Since the Bloch line continuously wraps around the cylindrical domain, it is defined as a skyrmion with winding number $S = 1$ [2,3]. If the Bloch line wraps continuously in a clockwise fashion, then it has helicity $\gamma = -\pi/2$, whereas if the Bloch line wraps in a counterclockwise direction, it has helicity $\gamma = +\pi/2$ [2]. At $H_z = 1450$ Oe, the skyrmions have a diameter of $\sim$71 nm, and their size does not vary significantly from initial formation to annihilation. The enclosed/enlarged region, detailed by red boxes in Figs. 1(d) and 1(e), shows the extremities of a stripe domain collapsing into a skyrmion [Fig. 1(f)], as well as the color/vector map representation of the magnetic textures enclosed. At this magnetic field strength, the domain morphology consists of a combination of disordered stripe domains and skyrmions [Figs. 1(c) and 1(d)]. As the magnetic field is further increased, the entire film fills with dipole skyrmions with equal populations of the two possible helicities [Figs. 1(g) and 1(h)]. The two different helicities ($S = 1, \gamma = \pm\pi/2$) appear as dark and light cylindrical textures in Fig. 1(g), and they arrange into a weakly ordered hexagonal lattice [Figs. 1(g) and 1(h)]. This skyrmion lattice is stable for a wide range of magnetic fields spanning from 1700 to 2400 Oe. By increasing the magnetic field further, the skyrmion lattice dissociates into a disordered isolated skyrmion states, where these textures begin to collapse as the film reaches magnetic saturation [Figs. 1(j) and 1(k)].

B. Temperature dependence of the skyrmion phase

Using a combination of real and reciprocal space imaging techniques, we explored the dependence on temperature and applied magnetic fields that results in the formation of the skyrmion phase for two Fe-Gd compositions. From scattering patterns obtained by means of resonant SXS (see Supplemental Material, Section A [46]), we identified four regions emphasizing long-range ordered magnetic states including: (i) disordered stripe domains, (ii) a stripe-to-skyrmion transition, (iii) a skyrmion lattice, and (iv) uniform magnetization. Then, using images obtained from Lorentz TEM and transmission soft x-ray microscopy, we supplemented our findings in the magnetic phase map. From real space images, we identified an additional region detailing (v) disordered skyrmions that occurs after the skyrmion lattice dissociates. Since disordered skyrmions do not have any long-range order, this region is not easily determined in scattering experiments.

Figure 2 summarizes the various magnetic domain configurations observed when an applied field, perpendicular to the film, is applied from zero field to magnetic saturation at detailed temperatures from 300 K to 50 K. We find that the [Fe (0.34 nm)/Gd (0.4 nm)] $\times$ 80 multilayer exhibits a similar domain morphology, as previously described with Lorentz TEM, with a skyrmion lattice that extends from room

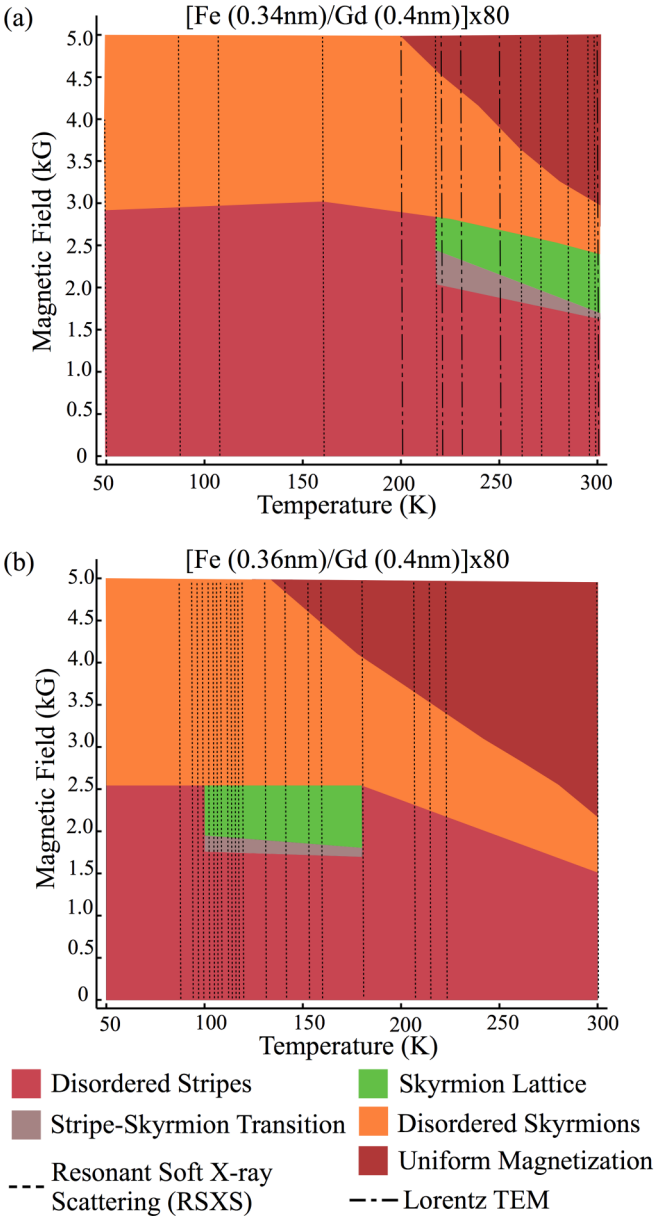

FIG. 2. Magnetic field and temperature dependence of the skyrmion phase. The magnetic phase diagrams for two Fe/Gd film structures are shown: (a) [Fe (0.34 nm)/Gd (0.4 nm)] $\times$ 80 exhibits a broad skyrmion phase around room temperature, and (b) [Fe (0.36 nm)/Gd (0.4 nm)] $\times$ 80 shows a similar skyrmion phase that is shifted to lower temperatures. These magnetic phase maps were constructed using data from four different imaging techniques: resonant soft x-ray scattering, Lorentz TEM, and transmission x-ray microscopy (at room temperature only). The marker lines detail the temperature and imaging technique used to scan the domain morphology.

temperature to 220 K for a wide range of applied magnetic fields [Fig. 2(a)]. At temperatures where no skyrmion phase exists, the Fe/Gd film primarily exhibits disordered stripe domains. In the case where we modified the Fe content of the Fe/Gd structure to [Fe (0.36 nm)/Gd (0.4 nm)] $\times$ 80, we find a similar broad skyrmion phase that is shifted to lower temperatures, spanning a temperature window from 180 K to

100 K [Fig. 2(b)]. Here, it is evident that the formation of a skyrmion phase is sensitive to the Fe/Gd composition and is tunable to a temperature range of interest.

C. Thickness dependence on stabilizing skyrmions

To further explore the formation of a skyrmion lattice at room temperature, we varied the number of Fe/Gd bilayer repetitions in the multilayer to investigate the role of the thin film magnetostatic energy on the skyrmion phase. The multilayer studied consisted of [Fe (0.34 nm)/Gd (0.41 nm)] × N, where $N = 40$, 80, and 120 repetitions, and where only the latter two film structures exhibited evidence of perpendicular magnetized stripelike domains in their magnetic hysteresis loops (see Supplemental Material, Section B [46]); however, [Fe (0.34 nm)/Gd (0.41 nm)] × 40 appears consistent with in-plane magnetic domains. This suggests that as the number of bilayers is increased, we gain magnetostatic energy to form perpendicular magnetic domains. Similar observations of a thickness driven spin reorientation of the magnetization, from in-plane to perpendicular, with increasing thickness have been reported for numerous systems, including hexagonal close-packed (hcp)(0001) Co films [42,43].

When examining the field dependence of the domain morphology by means of transmission soft x-ray microscopy measured at the Fe L_3 (708 eV) absorption edge, we verified that the $N = 40$ film does not show any perpendicular magnetic domains, while the $N = 80$ and $N = 120$ repeat films exhibited both stripe and skyrmion magnetic domain textures consistent with Fig. 1. The [Fe (0.34 nm)/Gd (0.41 nm)] × 80 film exhibits stripe domains at zero applied field where the contrast is sensitive to the out-of-plane magnetization [unlike Lorentz TEM, which is sensitive to the in-plane magnetization; Fig. 3(a)]. Here, domains with magnetization parallel/antiparallel to the perpendicular direction appear as dark/white textures. The presence of a small remanent in-plane magnetic field in the measurement causes the stripe domains to align in the direction of this field. With a modest out-of-plane field ($H_z = 500$, 625 Oe), we observe the stripes begin to pinch into cylindrical textures that occupy the same physical space as the original stripe [Figs. 3(b) and 3(c)]. At this field, there is a near equal population of stripes and aligned cylindrical domains. When the field is further increased ($H_z = 750$ Oe), we find all the stripes have pinched into aligned cylindrical textures that do not arrange into a close packing lattice [Fig. 3(d)]. As the field is further increased, the cylindrical domains dissipate [Fig. 3(d)], and we are left with the cylindrical textures that first formed [Figs. 3(b) and 3(c)]. This suggests that we observe two different magnetic domains as a consequence of the in-plane field. In one case, the Bloch line of most stripes aligns in the direction of the in-plane field, which results in the formation of magnetic bubbles (zero chirality) when a perpendicular field is applied as described in Ref. [16]; however, stripes with random Bloch-line arrangement result in skyrmions (chiral textures), as we have previously shown. Specifically, we have shown a skyrmion molecule [16] is made up of a bound pair of opposite helicity skyrmions, which can also be stabilized in Fe/Gd films as a result of applying a fixed in-plane field and then applying a perpendicular magnetic field.

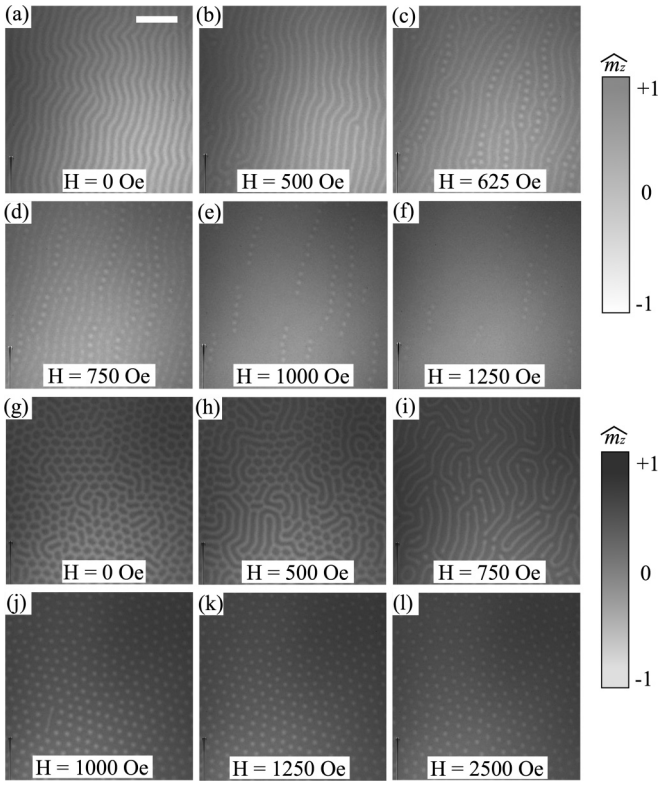

FIG. 3. Film thickness dependence of [Fe (0.34 nm)/Gd (0.41 nm)] × N. The domain morphology, obtained by x-ray microscopy, for Fe/Gd multilayers with different bilayer repetitions is detailed as a perpendicular magnetic field is applied from zero field to magnetic saturation. (a–f) [Fe (0.34 nm)/Gd (0.41 nm)] × 80 exhibits stripe domains at zero field (a) that pinch off into skyrmions as the magnetic field is increased (b–c). Above $H_z = 750$ Oe, the cylindrical textures begin to collapse in aligned clusters (e–f) until no skyrmions can be observed in the field of view. (g–l) [Fe (0.34 nm)/Gd (0.41 nm)] × 120 exhibits disordered stripe domains at zero field (g) that begin to collapse into skyrmions as the magnetic field is increased (h). These skyrmions arrange into an hcp lattice from $H_z = 800$ Oe to 2500 Oe (j–l). The scale bar in (a) corresponds to 1 μm.

The thickest film studied, [Fe (0.34 nm)/Gd (0.41 nm)] × 120, showed disordered stripe domains (white domains) and dumbbell domains (dark domains) at zero field. Here, the remanent in-plane field was insufficient to cause the stripes to order, as observed previously. When a perpendicular field was applied, the dumbbell domains began to merge to form disordered stripes [Fig. 3(h)], and by $H_z = 750$ Oe, the stripes with magnetization opposite to the field began to collapse into skyrmions [Fig. 3(i)]. By slightly increasing the field again, all the stripes collapsed into skyrmions, and these were arranged into a weakly coupled hexagonal lattice which spanned from $H_z = 800$ Oe to 2500 Oe [Figs. 3(j)–3(l)]. We found that the skyrmions have a diameter of ∼70 nm and that the size does not vary significantly from their initial formation to annihilation. The variation of film thickness clearly demonstrates that skyrmions, like bubbles, require a specific ratio of magnetic properties and film thickness for these magnetic textures to become favorable [25,27].

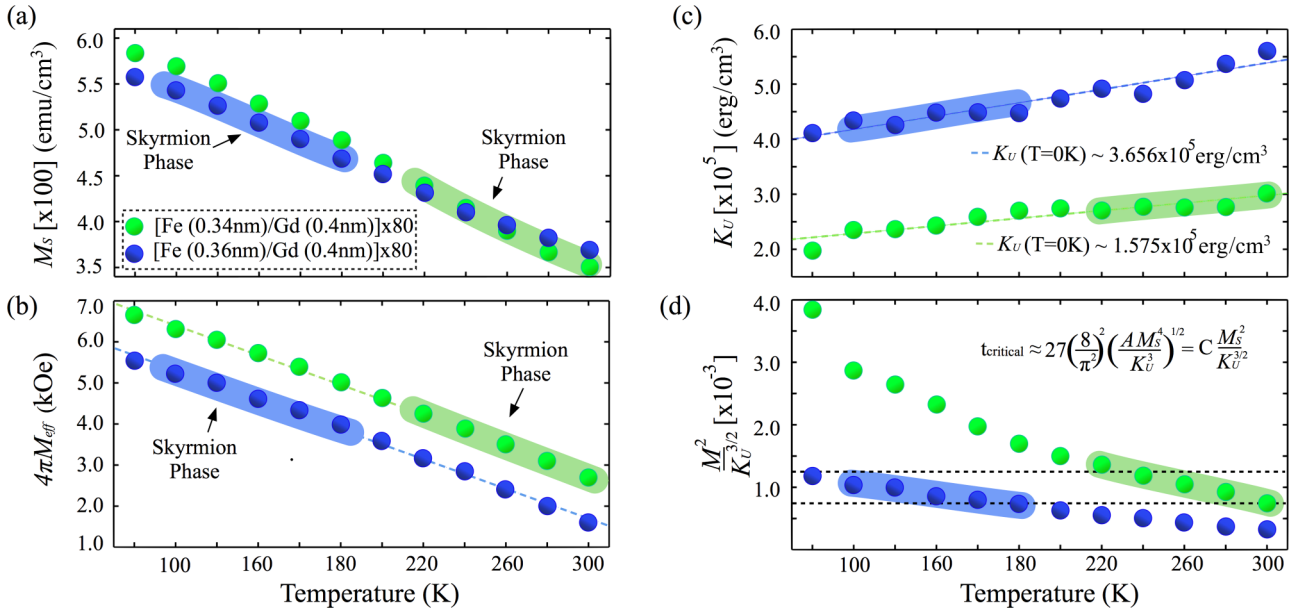

FIG. 4. Temperature-dependent magnetic and ferromagnetic resonance properties. The magnetization (a), effective magnetization (b), uniaxial anisotropy (c), and the $M_S^2/K_U^{3/2}$ ratio (d) are shown for [Fe (0.34 nm)/Gd (0.4 nm)] × 80 and [Fe (0.36 nm)/Gd (0.4 nm)] × 80. The region in temperature where each Fe/Gd film exhibits a skyrmion phase has been shaded to serve as a guide to the eye. By linearly fitting the uniaxial anisotropy with temperature, we can conclude that K_U is positive at absolute zero (c). The enclosed region with dashed lines in (d) represents a window of $M_S^2/K_U^{3/2}$ values where both Fe/Gd films exhibit a skyrmion phase.

D. Magnetic and ferromagnetic resonance properties

To determine the magnetic properties of the films in which skyrmion lattice formation becomes favorable [Figs. 2(a) and 2(b)], we performed temperature dependent magnetometry and ferromagnetic resonance (FMR) measurements. From magnetic hysteresis loops (Supplemental Material, Section B [46]) measured both by magnetometry and magneto-optical Kerr effect measurements, we determined that the Fe/Gd ferrimagnetic moment is Gd rich for these films at all measurement temperatures. This is consistent with measurements of bulk alloys with similar compositions. Both Fe/Gd films showed a relatively low magnetic moment that varied similarly with decreasing temperature [Fig. 4(a)]. The slightly stronger dependence of M_S vs T for the [Fe (0.34 nm)/Gd (0.4 nm)] × 80 film is also consistent with the lower Fe content, which leads to a higher low-temperature moment and lower T_C compared to the higher Fe content films. At temperatures where the Fe/Gd films exhibit a skyrmion phase, the magnetic moments are similar [Fig. 4(a)], which does not explain the shift of the skyrmion phase to a different temperature range (Fig. 2).

To characterize the anisotropy, FMR measurements were performed with perpendicular fields above magnetic saturation (Supplemental Material, Section B [46]). The resonance fields varied linearly with applied magnetic field, as expected from the Kittel formula [50], $f = \frac{\gamma_e}{2\pi}(H_{dc} - 4\pi M_S + H_K)$, where γ_e is the e^- gyromagnetic ratio, H_{dc} is the applied field, $4\pi M_S$ is the demagnetization field, *ok* is the saturation magnetization, and $H_K = 2 \cdot K_U/M_S$ is the perpendicular anisotropy field, where K_U is the uniaxial perpendicular anisotropy that is developed in the thin film growth process. The intercept with the field axis when frequency becomes zero is given when $H_{dc} = 4\pi M_S - H_K = 4\pi M_{eff}$. For all of our films, the intercept is positive (Supplemental Material, Section B [46]), indicating a relatively weak induced perpendicular anisotropy such that $K_U < K_D = 2\pi M_s^2$ or $Q = K_U/K_D < 1$, so the effective anisotropy is in-plane. The extracted values for M_S, $4\pi M_{eff}$, and K_U are given in Figs. 4(a)–4(c), respectively, as a function of temperature. As the temperature is reduced, both M_S and $4\pi M_{eff}$ increase roughly linearly with temperature, which suggests the films become more in-plane [Fig. 4(a) and 4(b)], while a modest decrease of the intrinsic perpendicular anisotropy is observed with decreasing temperature [Fig. 4(d)]. This atypical temperature dependence of the intrinsic anisotropy has been previously reported for rare-earth-rich Fe/Gd films with a small bilayer periodicity $t_{Fe} + t_{Gd} \leqslant 1.4$ nm (the Fe/Gd films detailed in this work have a period <0.8 nm) [51,52]. The increase in anisotropy with increasing Fe layer thickness is observed in a series of films and appears to be a general feature of the Fe/Gd system. Figure 4 further indicates the regions in temperature where we observed the skyrmion lattice phase.

The fact that domains and skyrmion lattices are only observed for film thickness above a critical thickness is consistent with earlier studies of films where $K_U < K_D$ [41–45]. There are theoretical estimates for the critical thickness for the onset of weak stripe domains, given by Refs. [42,44]:

$$t_1 \sim 17.7\sqrt{A}\, M_S^2/K_U^{3/2}, \quad (1)$$

where A is the exchange parameter. The predicted value for the thickness for the magnetization rotating from in plane to out of plane with stripe domains is given by Refs. [29,42,45]:

$$t_2 \sim 27.2\sqrt{A}\, M_S^2/K_U^{3/2}. \quad (2)$$

In both cases, the critical thickness scales as $M_S^2/K_U^{3/2}$. In Fig. 4(d), we plot this ratio as a function of temperature. We see that this ratio increases with decreasing temperature, reflecting the strong temperature dependence of the saturation magnetization. We also find that we experimentally observe the skyrmion phase for the same range of this ratio from 0.735×10^{-3} to 1.359×10^{-3}, as shown in Fig. 4(d). While neither of the values for M_S or K_U appears to be predictive for determining the temperature range where we observe the skyrmion, the ratio $M_S^2/K_U^{3/2}$ does provide a guideline for the formation of the skyrmion phase for the Fe/Gd system.

The only material parameter in Eqs. (1) and (2) we do not have a quantitative measure of is the exchange stiffness constant A; however, a qualitative measure can be deduced from noting that no superlattice peaks are observable in small-angle x-ray reflectometry (Supplemental Material, Section C [46]). This suggests that there is strong intermixing between the Fe and Gd layers; as a consequence, we can assume the Fe/Gd films are layered alloylike structures that resemble Fe-Gd alloys of similar composition. For this reason, we assume an exchange stiffness A between 2 and 5×10^{-7} erg/cm, based on values reported for similar Fe-Gd alloys [53–56]. Using these values of A, we would predict a t_1 in the range

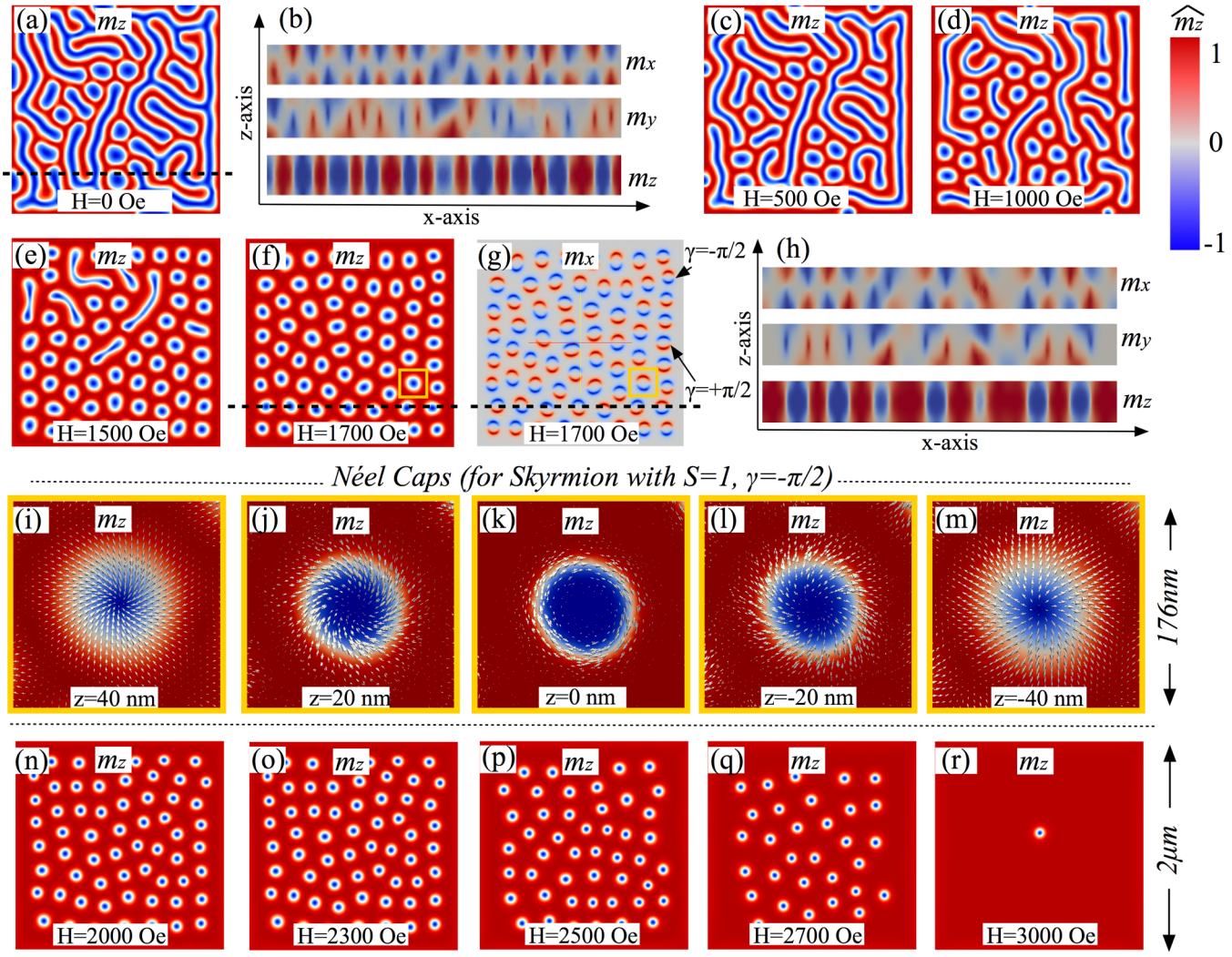

FIG. 5. Micromagnetic modeling of domain morphology. (a–r) [$M_S = 400\,\text{emu/cm}^3$, $K_U = 4 \times 10^5\,\text{erg/cm}^3$, and $A = 5 \times 10^{-7}\,\text{erg/cm}$]. The equilibrium states illustrate the field-dependent domain morphology at several magnetic fields that capture the domain evolution from a stripe to a skyrmion phase. These equilibrium states primarily depict the top side view of the magnetization along the z axis (m_z) at the top surface of the slab ($z = 40\,\text{nm}$). The magnetization (m_z) is represented by regions in red ($+m_z$) and blue ($-m_z$), whereas the in-plane magnetization (m_x,m_y) is represented by white regions surrounding the blue features. (b, h) Panels illustrating the lateral magnetization components (m_x,m_y,m_z) across the film thickness for the disordered stripe domains in (a) and the skyrmion phase in (f, g) along the dashed line. Inspection along the lateral magnetization reveals a Bloch-like wall configuration with closure domains in both states. The chirality of the skyrmions is depicted in (g) along the top side view of m_x across the center of the slab. (i–m) Detail of the magnetization distribution at different depths ($z = 40$, 20, 0, -20, -40 nm) for a skyrmion with chirality $S = +1$, $\gamma = -\pi/2$ that is enclosed in a box in (f, g). At each depth, the perpendicular magnetization is represented by blue ($-m_z$) and red ($+m_z$) regions and the in-plane magnetization distribution (m_x and m_y) is depicted by white arrows. The white arrows illustrate how the magnetization of the closure domains and Bloch line arrange at different depths of the slab. (n–r) Detail of the field evolution from ordered skyrmions to disordered skyrmions.

50.2 nm $< t_1 <$ 79.4 nm, which is in reasonable agreement for the transition from the in-plane to stripe phase between 40 and 80 repeats as observed experimentally.

E. Micromagnetic modeling

To understand the mechanism stabilizing the skyrmion phase, we performed numerical simulations of the Landau-Lifshitz-Gilbert (LLG) equation, utilizing the FASTMag [57] solver for a magnetic slab that is 2000 nm × 2000 nm × 80 nm. The input magnetic parameters were obtained from experiment (for further details, see figure captions). Figure 5 shows the field evolution of equilibrium states that results for $M_S = 400\,\text{emu/cm}^3$, $K_U = 4 \times 10^5\,\text{erg/cm}^3$, and $A = 5 \times 10^{-7}\,\text{erg/cm}$. These values are within the range of magnetic properties of both [Fe (0.34 nm)/Gd (0.4 nm)] × 80 and [Fe (0.36 nm)/Gd (0.4 nm)] × 80 (Fig. 4). Initially, the slab is saturated along the z axis, and then the perpendicular field is reduced to zero field. At any field step, the slab is allowed 30 ns to relax into an equilibrium state. Figures 5(a) (top view) and 5(b) (side view) are the results at zero field that exhibit a configuration of disordered stripe domains similar to those observed in Fig. 1. The typical domain periodicity is ∼183 nm. The cross-section view of the magnetization across the film thickness along the line given in Fig. 5(a) reveals a Bloch-like wall configuration at the center of the slab [Fig. 5(b), m_y component], while near the top and bottom of the film, there are flux closure caps [Fig. 5(b), m_x component]. This domain arrangement is expected given the low Q factor ($Q \sim 0.4$) as previously determined by resonant x-ray scattering from Fe/Gd films [49].

When a magnetic field is applied perpendicular to the slab, the stripe domain with magnetization opposite to the field direction collapses into individual skyrmions [Figs. 5(c)–5(e)]. As the magnetic field is increased further, the chiral textures arrange into a hexagonal lattice that exists from $H_{dc} = 1700$ Oe to 2300 Oe [Figs. 5(f), 5(g), and 5(n)–5(r)]. The typical skyrmion size is ∼83 nm, and the separation is given by ∼128 nm at $H_{dc} = 1700$ Oe. As the magnetic field is increased, the skyrmion size decreases to 53 nm at $H_{dc} = 2700$ Oe. The skyrmion size, separation, and field history are in good agreement with our experimental observation. For Figs. 5(a), 5(c)–5(g), and 5(n)–5(r), we plot the m_z component for magnetization, which can be compared to the contrast in Fig. 3.

For the skyrmions that form in Fig. 5, the domain walls are Bloch-like in the center of the film, and we find a roughly 50% chance of the two helicities. This can be seen in Fig. 5(g), where we plot the m_x component of magnetization at the center of the slab for $H_{dc} = 1700$ Oe. The skyrmions where the m_x component is red above the skyrmion and blue below have one circulation of the domain wall, and we characterize it by a winding number $S = 1$, $\gamma = -\pi/2$. The skyrmions where the m_x component is blue above the skyrmion and red below have the opposite circulation, and we characterize it by a winding number $S = 1$, $\gamma = \pi/2$. These results agree with the Lorentz TEM images of Fig. 1. By tracking the orientation of the in-plane components of the domain walls in Fig. 5 with increasing applied field, we find that the chirality of the skyrmions is determined by the chirality of the walls of the original domain. There are also examples of bubbles that form where the m_x component is either red or blue both above and below the bubble, and we characterize this by a winding number $S = 0$. Such bubbles are also observed in Lorentz TEM experiments.

Figure 5(h) shows the magnetic projection through the thickness of the film for the dashed line shown in Figs. 5(f) and 5(g). The m_z projection shows that the core of the skyrmion extends through the thickness of the film but narrows slightly near the top and bottom of the film. The m_y projection shows the circulating Bloch walls around each skyrmion and the m_x projection shows the existence of closure domains at the top and bottom of the films [this is shown in more detail in Figs. 5(i)–5(m)]. These closure domains will not be seen in the experimental images in Figs. 1 and 3 because both Lorentz TEM and transmission x-ray microscopy average over of the thickness of the film. As seen in Fig. 5(h) the closure domains have opposite signs at the top and bottom of the films and will average out in a transmission experiment.

The details of the domain-wall structure for one $S = 1$, $\gamma = -\pi/2$ skyrmion are shown in Figs. 5(i)–5(m). Shown are slices for different depths within the slab where the color gives m_z and the arrows give the direction of the in-plane magnetic component, and their length corresponds to the magnitude of the m_x and m_y components. At the center of the slab ($z = 0$ nm), m_x and m_y continuously wrap around the skyrmion, forming a Bloch wall, and the wall width is the narrowest. As one progresses towards the top ($z = 40$ nm) or bottom ($z = -40$ nm) surface, the domain wall broadens and becomes more Néel like. At the top surface, the in-plane magnetization points mostly radially in forming the Néel caps. At the bottom surface, the in-plane magnetization now points away from the skyrmion center. For a skyrmion with opposite helicity, the wrapping of m_x and m_y toward the center of the skyrmion core is inverted, while the Néel cap configuration at the top and bottom of the slab is the same.

For higher fields, the skyrmions become disordered and begin to disappear, first at the edges and then throughout the film as the field approaches magnetic saturation [Figs. 5(n)–5(r)]. Overall, the field-dependent domain morphology is in good agreement with our experimental observations. Here, the micromagnetic model suggests the chiral bubble domains form due to minimization of competing demagnetization energy and domain wall energy, and that thermal fluctuations are not required for their formation since this is a zero-temperature model. To compare our numerical results to our experimental observations of chiral cylindrical textures, we computed the magnetization projection averaged over the film thickness. This is shown in Fig. 6 for $\langle m_z \rangle$ and $\langle m_x \rangle$, and these values are compared to selected Lorentz TEM and x-ray images. There is no signature of the different helicities of $\langle m_z \rangle$, as expected and consistent the x-ray images. The $\langle m_x \rangle$ and $\langle m_y \rangle$ projection is only sensitive to the Bloch nature of the wall, as seen in Lorentz TEM.

Next, we discuss the magnetic properties required to stabilize a dipolar field driven skyrmion phase. As we have demonstrated, the composition of the Fe/Gd specimen directly correlates to the temperature and applied magnetic field range in which skyrmions become favorable, particularly in a window of $M_S^2/K_U^{3/2}$ values. To understand the effect of exchange A in the formation of a skyrmion phase, we

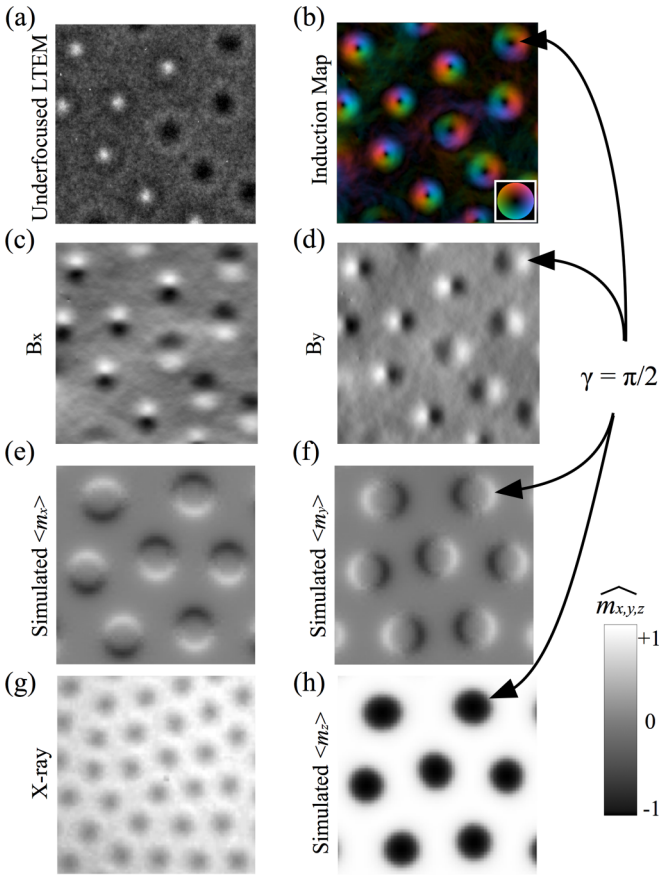

FIG. 6. Comparison between numerical and experimental observation of skyrmions. (a, b) Underfocused Lorentz TEM image and its corresponding magnetic induction map illustrate the Bloch-line arrangement of the skyrmions. (c, d) The individual in-plane components of the magnetic induction B_x and B_y are obtained from (b). (e, f) Detail of a numerical computed average magnetization across the slab for $\langle m_x \rangle$ and $\langle m_y \rangle$. (g) Transmission x-ray microscopy image of the skyrmion phase solely shows the presence of cylindrical domains, which resemble the average magnetization across the slab for $\langle m_z \rangle$ in (h). A skyrmion with $S = 1$, $\gamma = \pi/2$ is referenced to directly compare experimental and numerical results in (b, d, f, h). The scale bar references the micromagnetic domain states.

simulated magnetic domains similar to those in Fig. 5 for a fixed applied field $H_z = 2000$ Oe and $M_S = 400\,\text{emu/cm}^3$ and various K_U and A values, as shown in Fig. 7(a). We find that modest changes in either of these parameters leads to different equilibrium states. For instance, as K_U is increased, the skyrmion lattice quickly becomes less correlated, and the skyrmion size begins to vary. Increasing the exchange A, for any fixed K_U except $K_U = 2 \times 10^5\,\text{erg/cm}^3$, results in a skyrmion arrangement that becomes more disordered. For a fixed M_S, a close packing lattice of skyrmions is only achievable in a narrow region of both K_U and A. Our modeling suggests a modest value of the exchange parameter is a critical parameter that determines the long-range order of skyrmions forming a lattice, and it supports the existence of a weak exchange in these Gd-rich Fe/Gd films.

IV. DISCUSSION

Using a combination of numerical simulations and experimental data, we constructed a K_U-M_S phase map (for a fixed $A = 5 \times 10^{-7}\,\text{erg/cm}$) that illustrates the measured and calculated magnetic domains at zero field and applied field values [Fig. 7(b)]. In the phase map, the Q ratio is also plotted in the foreground with contour lines depicting variations in $Q = K_U/2\pi M_S^2$ for domain states with $Q < 1$. The Q ratio serves as a heuristic to estimate volume fraction distributions of perpendicular domains and Néel caps in these thick Fe/Gd films. We recall that when films exhibit a Q ratio greater than 1, the domain morphology favors perpendicular domains with negligible Néel caps; likewise, as Q decreases below 1, the volume fraction of the Néel caps grows, and the perpendicular domains occupy a lower volume fraction.

Inspecting the domain states when the anisotropy is very low ($K_U \leqslant 2 \times 10^5\,\text{erg/cm}^3$) such that the thickness is below t_1 (Eq. (1)), we find the magnetization is in plane, and as a result of the geometry of the slab, the system favors the formation of an in-plane vortex configuration. For larger K_U (or lower M_S), the film transitions to out-of-plane magnetic domains. The two predominant magnetic configurations consist of labyrinth domains at zero field that form skyrmions when a field is applied perpendicular to the slab. What differentiates the regions are the mechanisms by which the skyrmions form; in one case, (i) the stripes pinch off into chiral bubbles as seen in Fig. 5, and in the other, (ii) the extremities of the stripe collapse to form single chiral bubbles that do not arrange in a lattice as seen in Co/Pt multilayers [58], for instance. We observe the skyrmions arranging in a close packing lattice for only a small region of K_U and M_S values; in addition, this region exists at Q value ratios from 0.2 to 0.4, which suggests the overall domain structure of perpendicular domains and Néel caps is fairly comparable. As we move away from the skyrmion lattice region, the distance between the cylindrical textures increases until they become disordered.

In the foreground of Fig. 7(b) we also detail the range of $M_S^2/K_U^{3/2}$ values where an ordered skyrmion phase is observable numerically and experimentally. Equilibrium states within this region of varying M_S and K_U will share similar critical thickness t_1, for a fixed A, at which weak perpendicular stripe domains will form, but only a small region of low M_S and K_U results in a close packing lattice of skyrmions. Large M_S and K_U result in stripe domains that form disordered chiral bubbles. This suggests that the critical thickness is not a sole determinate of ordered skyrmions.

The Lorentz TEM images (Fig. 1) and numerical simulations (Figs. 5 and 6) suggest that the stabilization of these skyrmions is purely driven by competing dipolar and exchange energies and that no DMI is present in these films. The Lorentz TEM images show two helicity textures with an equal population distribution in the skyrmion phase. If some DMI were present, then the system would likely favor the formation of a chiral domain compared to the other, as well as a Néel cap orientation over the other, which is not the case here. The fact that we numerically observe the stabilization of the same two-helicity skyrmions on a slab with no DMI supports this observation. Given the nature of these skyrmions, these films could potentially also be designed to host antiskyrmions, as

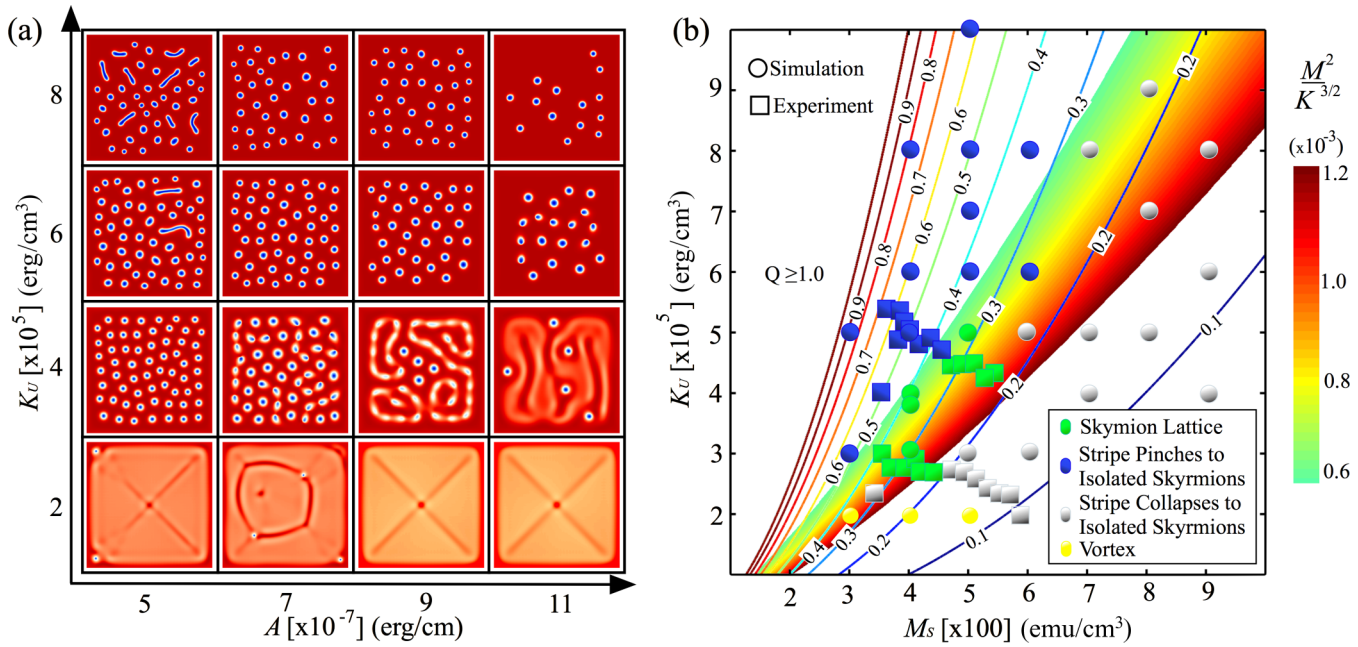

FIG. 7. Skyrmion phase stability in magnetic property phase maps. (a) The top side view of equilibrium states that form at $H_z = 2000$ Oe investigated under different ratios of K_U and A for a fixed $M_S = 400$ emu/cm^3. These equilibrium states detail the magnetization along the z axis (m_z) at the top surface of the slab ($z = 40$ nm). The magnetization (m_z) is represented by regions in red ($+m_z$) and blue ($-m_z$), whereas the in-plane magnetization (m_x,m_y) is represented by white regions surrounding the blue features. (b) The formation of a skyrmion lattice explored in terms of varying M_S and K_U for a fixed $A = 5 \times 10^{-7}$ erg/cm using a combination of experimental results (□) and simulations (○). Contour lines detail the corresponding Q factor in this magnetic phase region, which denotes the balance between anisotropy energy K_U and magnetostatic energy $2\pi M_S^2$. For details pertaining to the simulation parameters, see Methods.

recently theoretically predicted [59]. Unlike bubble domains, which are typically observed in materials with $Q > 1$ and exhibit strong PMA, our chiral cylindrical domains appear in a material parameter space where $Q < 1$, and the formation of perpendicular domains results from a thickness-driven domain morphology rearrangement [41–45].

In conclusion, we have demonstrated the existence of skyrmion lattice in Fe/Gd films by means of real and reciprocal space imaging techniques. We have shown that by tuning the magnetic properties and film thickness, we can control the stabilization of a skyrmion phase in temperature and applied magnetic fields. The simplicity of the magnetic material and the easily tunable properties make these films an interesting potential test bed for studying the physics of dipole skyrmions, as well as for potential memory technologies. Furthermore, the universality of our numerical model presents a roadmap to design new classes of materials that can exhibit dipolar field–driven skyrmions.

ACKNOWLEDGMENTS

Work at University of California–San Diego, including materials synthesis and characterization, participation in synchrotron measurements, and modeling, was supported by U.S. Department of Energy (DOE), Office of Basic Energy Sciences (BES) under Award No. DE-SC0003678. Work at University of Oregon was supported by the DOE, Office of Science, BES under Award No. DE-SC0010466. Work at the Advanced Light Source, Lawrence Berkeley National Laboratory (LBNL), was supported by the Director, Office of Science, BES, of the DOE (Contract No. DE-AC02- 05CH11231). S.A.M. acknowledges support from the Department of Defense (DoD) through the Science, Mathematics & Research for Transformation (SMART) Scholarship. B.J.M. and J.J.C. gratefully acknowledge the use of CAMCOR facilities, which have been purchased with a combination of federal and state funding. M.-Y.I. acknowledges support by Leading Foreign Research Institute Recruitment Program through the National Research Foundation (NRF) of Korea funded by the Ministry of Education, Science and Technology (MEST) (Grants No. 2012K1A4A3053565 and No. 2014R1A2A2A01003709). S.D.K. and P.F. acknowledge support by the Director, Office of Science, BES, Materials Sciences and Engineering Division, of the DOE under Contract No. DE-AC02-05-CH11231 within the Nonequilibrium Magnetic Materials Program (No. KC2204) at LBNL.

[1] T. H. R. Skyrme, Nuclear Phys. **31**, 556 (1962).
[2] N. Nagaosa and Y. Tokura, Nat. Nanotech. **8**, 899 (2013).
[3] H.-B. Braun, Adv. Phys. **61**, 1 (2012).
[4] S. P. Parkin, M. Hayashi, and L. Thomas, Science **320**, 190 (2008).

[5] N. S. Kiselev, A. N. Bogdanov, R. Schafer, and U. K. Robler, J. Phys. D: Appl. Phys. **44**, 392001 (2011).
[6] A. Fert, V. Cros, and J. Sampaio, Nature Nanotech. **8**, 152 (2013).
[7] S. Mühlbauer, B. Binz, F. Jonietz, C. Pfleiderer, A. Rosch, A. Neubauer, R. Georgii, and P. Böni, Science **323**, 915 (2009).
[8] W. Münzer, A. Neubauer, T. Adams, S. Mühlbauer, C. Franz, F. Jonietz, R. Georgii, P. Böni, B. Pedersen, M. Schmidt, A. Rosch, and C. Pfleiderer, Phys. Rev. B. **81**, 041203(R) (2010).
[9] X. Z. Yu, Y. Onose, N. Kamazawa, J. H. Park, J. H. Han, Y. Matsui, N. Nagaosa, and Y. Tokura, Nature **465**, 901 (2010).
[10] S. Seki, X. Z. Yu, S. Ishiwata, and Y. Tokura, Science **336**, 198 (2012).
[11] X. Z. Yu, N. Kanazawa, Y. Onose, K. Kimoto, W. Z. Zhang, S. Ishiwata, Y. Matsui, and Y. Tokura, Nat. Mater. **10**, 106 (2011).
[12] W. Jiang, P. Upadhyaya, W. Zhang, G. Yu, M. B. Jungfleisch, F. Y. Fradin, J. E. Pearson, Y. Tserkovnyak, K. L. Wang, O. Heinonen, S. G. E. te Velthuis, and A. Hoffmann, Science **349**, 283 (2015).
[13] C. Moreau-Luchaire, C. Moutafis, N. Reyren, J. Sampaio, C. A. F. Vaz, N. Van Horne, K. Bouzehouane, K. Garcia, C. Deranlot, P. Warnicke, P. Wohlhüter, J.-M. George, M. Weigand, J. Raabe, V. Cros, and A. Fert, Nat. Nanotech. **11**, 444 (2016).
[14] S. Woo, K. Litzius, B. Krüger, M.-Y. Im, L. Caretta, K. Richter, M. Mann, A. Krone, R. M. Reeve, M. Weigand, P. Agrawal, I. Lemesh, M.-A. Mawass, P. Fischer, M. Kläui, and G. S. D. Beach, Nat. Mat. **15**, 501 (2016).
[15] W. Wang, Y. Zhang, G. Xu, L. Peng, B. Ding, Y. Wang, Z. Hou, X. Zhang, X. Li, E. Liu, S. Wang, J. Cai, F. Wang, J. Li, F. Hu, G. Wu, B. Shen, and X.-X. Zhang, Adv. Mater. **28**, 6887 (2016).
[16] J. C. T Lee, J. J. Chess, S. A. Montoya, X. Shi, N. Tamura, S. K. Mishra, P. Fischer, B. J. McMorran, S. K. Sinha, E. E. Fullerton, S. D. Kevan, and S. Roy, Appl. Phys. Lett. **109**, 022402 (2016).
[17] M. Finazzi, M. Savoini, A. R. Khorsand, A. Tsukamoto, A. Itoh, L. Duo, A. Kirilyuk, Th. Rasing, and M. Ezawa, Phys. Rev. Lett. **110**, 177205 (2013).
[18] X. Z. Yu, K. Shibata, W. Koshibae, Y. Tokunaga, Y. Kaneko, T. Nagai, K. Kimoto, Y. Taguchi, N. Nagaosa, and Y. Tokura, Phys. Rev. B **93**, 134417 (2016).
[19] X. Z. Yu, M. Mostovoy, Y. Tokunaga, W. Zhang, K. Kimoto, Y. Matsui, Y. Kaneko, N. Nagaosa, and Y. Tokura, Proc. Natl Acad. Sci. USA **109**, 8856 (2012).
[20] I. Dzyaloshinskii, J. Phys. Chem. Solids **4**, 241 (1958).
[21] T. Moriya, Phys. Rev. **120**, 91 (1960).
[22] S. Heinze, K. von Bergmann, M. Menzel, J. Brede, A. Kubetzka, R. Wiesendanger, G. Bihlmayer, and S. Blüger, Nature Phys. **7**, 713 (2011).
[23] T. Okubo, S. Chung, and H. Kawamura, Phys. Rev. Lett. **108**, 017206 (2012).
[24] C. Kittel, Rev. Mod. Phys. **21**, 541 (1949).
[25] C. Kooy and U. Enz, Philips Res. Rep. **15**, 7 (1960).
[26] Y. S. Lin, J. Grundy, and E. A. Giess, Appl. Phys. Lett. **23**, 485 (1973).
[27] J. A. Cape and W. Lehman, J. Appl. Phys. **42**, 13 (1971).
[28] A. Thiele, J. Appl. Phys. **41**, 1139 (1970).
[29] Z. Malek and V. Kambersky, Czech. J. Phys. **8**, 416 (1958).
[30] C. Kittel, Phys. Rev. **70**, 965 (1946).
[31] O. Hellwig, A. Berger, J. B. Kortright, and E. E. Fullerton, J. Magn. Magn. Mater. **319**, 13 (2007).
[32] M. Seul, L. O. Monar, L. O'Gorman, and R. Wolfe, Science **254**, 1616 (1991).
[33] M. Seul and R. Wolfe, Phys. Rev. A **46**, 7519 (1992).
[34] M. Seul and R. Wolfe, Phys. Rev. A **46**, 7534 (1992).
[35] A. P. Malozemoff, J. C. Slonczewski, and R. Wolfe, *Magnetic Domain Walls in Bubble Materials* (Academic Press, San Diego, CA, 1979), pp. 306–314.
[36] A. Hubert and R. Schäfer, *Magnetic Domains* (Springer, Berlin, 1998), pp. 499, 509.
[37] T. Suzuki, J. Magn. Magn. Mater. **31**, 1009 (1983).
[38] A. H. Eschenfelder, *Magnetic Bubble Technology* (Springer, Berlin, 1981), pp. 210–224.
[39] P. Chaudhari, J. J. Cuomo, and R. J. Gambino, Appl. Phys. Lett. **22**, 337 (1973).
[40] N. Sato and N. Habu, J. Appl. Phys. **61**, 4287 (1987).
[41] M. W. Muller, J. Appl. Phys. **38**, 6 (1967).
[42] M. Hehn, S. Padovani, K. Ounadjela, and J. P. Bucher, Phys. Rev. B **54**, 3428 (1996).
[43] D. M. Donnet, K. M. Krishnan, and Y. Yajima, J. Phys. D: Appl. Phys. **28**, 1942 (1995).
[44] N. Saito, H. Fujiwara, and Y. Sugita, J. Phys. Soc. Jpn. **19**, 1116 (1964).
[45] D. J. Craik and P. V. Cooper, Phys. Lett. A **41**, 255 (1972).
[46] See Supplemental Material at http://link.aps.org/supplemental/10.1103/PhysRevB.95.024415 for resonant soft x-ray scattering results, magnetic hysteresis and ferromagnetic resonance measurements and small angle x-ray reflectivity measurements from Fe/Gd specimens.
[47] M. R. Teague, J. Opt. Soc. Am. **73**, 1434 (1983).
[48] M. De Graef and Y. Zhu, *Magnetic Imaging and its Applications to Materials* (Academic Press, San Diego, CA, 2000), Vol. 36, pp. 58–68.
[49] J. Miguel, J. F. Peters, O. M. Toulemonde, S. S. Dhesi, N. B. Brookes, and J. B. Goedkoop, Phys. Rev. B **74**, 094437 (2006).
[50] C. Kittel, Phys. Rev. **73**, 155 (1948).
[51] E. Stavrou and E. Roll, J. Appl. Phys. **85**, 5971 (1999).
[52] E. Stavrou, R. Sbiaa, T. Suzuki, S. Knappmann, and K. Roll, J. Appl. Phys. **87**, 6899 (2000).
[53] C. Vittoria, P. Lubitz, and V. Ritz. J. Appl. Phys. **49**, 4908 (1978).
[54] Y. Mimura, N. Imamura, T. Kobayashi, A. Okada, and Y. Kushiro, J. Appl. Phys. **49**, 1208 (1978).
[55] M. Mansuripur and M. F. Ruane, IEEE Trans. Magn. Mag. **22**, 33 (1986).
[56] P. Lubitz, J. Schelleng, and C. Vittoria, Solid State Comm. **18**, 965 (1976).
[57] R. Chang, S. Li, M. V. Lubarda, B. Livshitz, and V. Lomakin, J. Appl. Phys. **109**, 07D358 (2011).
[58] J. E. Davies, O. Hellwig, E. E. Fullerton, G. Denbeaux, J. B. Kortright, and K. Liu, Phys. Rev. B. **70**, 224434 (2004).
[59] W. Koshibae and N. Nagaosa, Nat. Comm. **7**, 10542 (2016).